A combined theoretical and computational study of interstrand DNA guanine-guanine cross-linking by *trans*-[Pt(pyridine)$_2$] derived from the photoactivated prodrug *trans,trans,trans*-[Pt(N$_3$)$_2$(OH)$_2$(pyridine)$_2$]

SCHOLARONE™
Manuscripts

A combined theoretical and computational study of interstrand DNA guanine-guanine cross-linking by *trans*-[Pt(pyridine)₂] derived from the photoactivated prodrug *trans,trans,trans*-[Pt(N₃)₂(OH)₂(pyridine)₂]

Hui-Chung Tai,[†] Ralf Brodbeck,[†] Jana Kasparkova,[‡] Nicola J. Farrer,[†] Viktor Brabec,[‡] Peter J. Sadler[†]*, and Robert J. Deeth[†]*

Department of Chemistry, University of Warwick, Gibbet Hill Road, Coventry CV4 7AL, United Kingdom, and the Institute of Biophysics, Academy of Sciences of the Czech Republic, v.v.i., Kralovopolska 135, 61265 Brno, Czech Republic

[†] University of Warwick

[‡] Institute of Biophysics

*To whom correspondence may be addressed. E-mail: r.j.deeth@warwick.ac.uk, p.j.sadler@warwick.ac.uk.

1

Abstract: Molecular modeling and extensive experimental studies are used to study DNA distortions induced by binding platinum(II)-containing fragments derived from cisplatin and a new class of photoactive platinum anticancer drugs. The major photoproduct of the novel platinum(IV) prodrug *trans,trans,trans*-$[Pt(N_3)_2(OH)_2(py)_2]$ (**1**) contains the *trans*-$\{Pt(py)_2\}^{2+}$ moiety. Using a tailored DNA sequence, experimental studies establish the possibility of interstrand binding of *trans*-$\{Pt(py)_2\}^{2+}$ (**P**) to guanine N7 positions on each DNA strand. Ligand field molecular mechanics (LFMM) parameters for Pt–guanine interactions are then derived and validated against a range of experimental structures from the Cambridge Structural Database, published QM/MM structures of model Pt-DNA systems and additional DFT studies. Ligand field molecular dynamics (LFMD) simulation protocols are developed and validated using experimentally characterized bifunctional DNA adducts involving both an intra- and an interstrand crosslink of cisplatin. We then turn to the interaction of **P** with the DNA duplex dodecamer, $d(5\text{'}-C_1C_2T_3C_4T_5C_6G_7T_8C_9T_{10}C_{11}C_{12}-3\text{'}) \bullet d(5\text{'}-G_{13}G_{14}A_{15}G_{16}A_{17}C_{18}G_{19}A_{20}G_{21}A_{22}G_{23}G_{24}-3\text{'})$ which is known to form a monofunctional adduct with *cis*-$\{Pt(NH_3)_2(py)\}$. **P** coordinated to G_7 and G_{19} is simulated giving a predicted bend towards the minor groove. This is widened at one end of the platinated site and deepened at the opposite end, while the **P**-DNA complex exhibits a global bend of ~67° and an unwinding of ~20°. Such cross-links offer possibilities for specific protein–DNA interactions and suggest possible mechanisms to explain the high potency of this photoactivated complex.

2

Introduction

Since its serendipitous discovery, the anticancer drug cisplatin (*cis*-[Pt(NH$_3$)$_2$Cl$_2$]) has been widely used against various tumors.[1,2] This has stimulated the synthesis and biological evaluation of many platinum-based drugs and an exploration of other nearby elements from the periodic table.[3-5] Extensive research has been reported which elucidates cisplatin's mechanism of action.[2,6-10] Upon administration, the relatively high concentration of chloride ions in blood (~100 mM) maintains cisplatin in a neutral state. Inside the cell, the lower chloride ion concentrations (~4-20 mM) facilitate activation of cisplatin by stepwise aquation, and subsequent reaction with various cellular targets, most notably DNA. The interaction between platinated DNA and nuclear proteins induces signal transduction pathways which lead to DNA-damage recognition and repair, cell-cycle arrest, and apoptosis or necrosis.[11,12]

Experimental characterization of platinum–DNA adducts shows the presence of approximately 65% 1,2-d(GpG), 25% 1,2-d(ApG), and 5-10% 1,3-d(GpNpG) intrastrand cross-links as major components, although interstrand cross-links and monofunctional adducts have also been identified.[11] In all cases, platinum is bound to the N7 position of purine bases. Formation of cisplatin adducts significantly alters the structure of the target DNA by bending, unwinding, and destabilizing the duplex. The structural details of platinum-DNA adducts are available from X-ray and NMR studies, and from molecular mechanics simulation.[6,13-21] Although these Pt-DNA adducts exhibit some degree of structural similarity, arising from coordination to the N7 atom of the purine base, it is clear that each distorts the duplex DNA in a characteristic manner.[5,6] These nuances may activate distinctive DNA-damage recognition and cellular processes, which possibly mediate cytotoxicity and anticancer properties of the compounds via different mechanisms of action.[2,11,12]

The Pt^{IV} complex *trans,trans,trans*-[Pt^{IV}(N$_3$)$_2$(OH)$_2$(py)$_2$] (**1**) is stable in the dark, but has remarkable cytotoxicity when activated with a low-dose (5 J cm^{-2}) of visible light (420 nm). In the presence of 5'-GMP, the major photoproduct is *trans*-[Pt^{II}(py)$_2$(5'-GMP)$_2$]$^{2+}$ as confirmed by ^{1}H and ^{195}Pt NMR spectroscopy.[22] Photoactivation promotes the rapid formation of such *bis*-guanine adducts whereas in thermal reactions involving *trans* diamine

3

complexes, such *trans* cross-links are formed very slowly, if at all.[23] Thus, *trans*-GG crosslinks formed on DNA after photoactivation of *trans*-diazido Pt[IV] complexes would be unusual and may contribute to their high potency towards cancer cells.[24]

The detailed molecular mechanisms by which cells process interstrand cross-links are not understood. Recently, experiments have shown that formation of 1,2-d(GpG), and 1,3-d(GpTpG) intrastrand cisplatin–DNA adducts in the nucleosome core can alter nucleosome mobility[25] and/or positioning[26,27] and compounds with higher molecular weights display a greater tendency to target the linker region of nucleosomal DNA.[28] We report experimental studies involving a specially-designed sequence which confirm for the first time that the predicted *trans*-[Pt[II](py)$_2$(G)$_2$]$^{2+}$ interstand crosslink may be formed in significant amounts when complex **1** is photoactivated in the presence of DNA. However, while the experiments confirm it is possible to generate interstrand crosslinks, they do not provide detailed structural information. Hence, we turn to molecular modeling to gain further insights into the structure and mechanism of action of this novel platinum lesion.

Quantum mechanics (QM) is too expensive for large systems like proteins and DNA and classical techniques such as molecular mechanics (MM) and molecular dynamics (MD) are usually used.[29,30] However, MD simulations of metal-containing systems present significant challenges since the d electrons can have a potent effect on the structure and properties of coordination complexes. Treating the local coordination environment around the metal center quantum mechanically while the rest of the system is handled with MM (i.e. the QM/MM method) is becoming increasingly popular although the computational cost of the QM part remains a bottleneck. Alternatively, the flexibility and precision of quantum mechanics at the speed of molecular mechanics can be achieved by ligand field molecular mechanics (LFMM) which has been applied to the modeling of electronically 'difficult' metal ions such as d^9 Cu(II) and both spin states of d^8 Ni(II) centers for which conventional MM does not provide a general approach.[31-33] Polarizable[34] and solid state[35] versions of LFMM have been implemented and we have estimated that LFMM is up to four orders of magnitude faster than the density functional theory methods which often form the QM part of QM/M simulations.[36]

Conventional force fields have been applied to Pt-guanine binding using torsional constraints or out-of-plane deformation terms to ensure the Pt atom remains within the plane of the

4

coordinated purine. However, *ab initio* calculations,[37,38] suggest the platinum out-of-plane bending force constant is overestimated. Here, we first develop new LFMM parameters for guanine bound to platinum via N7, which, in combination with previous work on modeling of the *trans* influence in Pt(II) complexes,[38] reproduces experimental bond lengths and bond angles of small platinum complexes. The new parameters are then used in dynamics simulations of several Pt-DNA systems. For development and validation purposes, we consider the well-characterized 1,2-intrastrand and the interstrand cisplatin–DNA adducts in which *cis*-$\{Pt(NH_3)_2\}^{2+}$ is coordinated to the N7 atoms of guanine bases. For cisplatin, 1,2-intrastrand adducts are the major DNA products formed and are thought to be important for its anticancer activity, while the minor interstrand cross-links prevent DNA strand separation and can block DNA replication and/or DNA transcription and can be lethal to cells lacking the ability to remove the cross-link.[39] We then explore a putative **P**–DNA complex, based on the related $\{Pt(NH_3)(py)_2\}$ mono-functional adduct, but now with a bifunctional *trans*-$[Pt^{II}(py)_2(dGua)_2]^{2+}$ interstrand cross-link formed by binding of the major photoreduction product of **1** to two guanine nucleobases in DNA.

Computational details

To estimate partial charges of Pt-guanine complexes, the geometry of a model Pt-guanine complex (Figure 6, *vide infra*) was fully optimized using the Amsterdam Density Functional 2007 program (ADF)[40] with the BP86[41,42] functional in conjunction with Grimme's empirical correction for dispersion,[43] a triple-ζ plus double polarization basis set (TZ2P) on all atoms and a scalar ZORA[44] relativistic correction. To maintain compatibility with our previous parameterization, CHelpG[45] charges were computed (using the previously optimized structure) at the HF/6-31G(d) level using the Gaussian 03 program[46] with the LanL2DZ[47] basis set with an extra set of f functions using the exponents determined by Frenking *et al*. for the metal[48] with Pt given a van der Waals radius of 1.8 Å.

Ligand Field Molecular Mechanics (LFMM) uses a generalized ligand field theory calculation of the d-orbital energies to estimate the ligand field stabilization energy (LFSE).[33] The LFSE depends on the complex, the d configuration and the spin state and can have a

5

marked effect on a range of thermodynamic and structural properties. Since MM is inherently bond-centered, the most convenient form of ligand field model is the angular overlap model (AOM).[49] Each M-L interaction is parameterized in terms of local bonding modes of σ or π symmetry, with each assigned its own parameter (Figure 1).[25,26] The full ligand field potential is then constructed by summing the contributions from each bonding mode over all ligands and diagonalizing the resulting matrix. The LFSE and its gradients are then merged with a more-or-less conventional MM scheme.[50] The total potential energy, E_{tot} can be modeled by simple contributions from bond stretching, E_{str}, angle bending, E_{bend}, torsional twisting, E_{tor}, and non–bonding interactions, E_{nb}, where the latter may include both van der Waals and electrostatic terms. The core concept of the ligand field molecular mechanics (LFMM) method is the addition to the conventional potential energy expression of a new term specifically designed to describe the effects of the ligand field stabilization energy (LFSE):[31]

$$E_{tot} = \Sigma\, E_{str} + \Sigma\, E_{bend} + \Sigma\, E_{tor} + \Sigma\, E_{nb} + \text{LFSE} \tag{1}$$
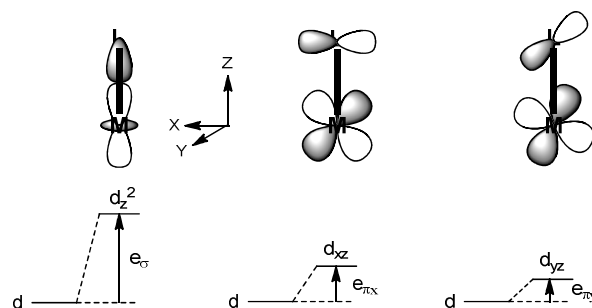
Figure 1. Definition of AOM parameters in terms of local M–L bonding.

In other words, LFMM merges conventional MM for the 'organic' parts of a transition metal complex with an AOM treatment of the LFSE for the metal center. Each molecule is divided into two overlapping regions as illustrated in Figure 2 for a $[M(en)_2]^{n+}$ complex. The coordination region contains the metal and its bonded donor atoms (e.g. the MN_4 unit) and the ligand region comprises everything except the metal atom (e.g. the ethylenediamine ligands). The LFMM routines focus on the coordination region and handle the LFSE, Pt–L bond stretching (via a Morse function) and L–Pt–L angle bending (via an explicit L-L

6

repulsive term). The program, 'd orbital molecular mechanics in the Molecular Operating Environment' (DommiMOE)[51,52], has been designed to take advantage of existing force fields implemented in MOE – e.g. MMFF[53-57], AMBER[58] and CHARMM[59] – which treat all the interactions in the ligand region.
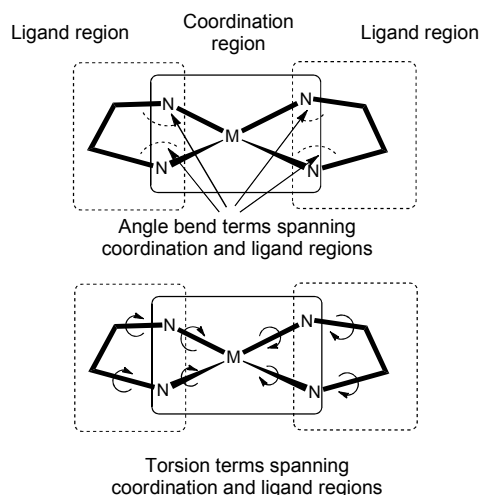
Figure 2: Schematic representation of division into coordination and ligand regions and force field terms which span the two.

DommiMOE LFMD simulations were carried out at physiological pH and a mean temperature of 300 K using the LFMM/AMBER94 force field. Electrical neutrality was ensured by adding sufficient sodium ions to neutralize the phosphate backbone negative charges.

Simulation 1 (Sim1) was on a 1,2-intrastrand cisplatin–DNA dodecamer d(5'-$C_1C_2T_3C_4T_5G_6*G_7*T_8C_9T_{10}C_{11}C_{12}$-3')• d(5'-$G_{13}G_{14}A_{15}G_{16}A_{17}C_{18}C_{19}A_{20}G_{21}A_{22}G_{23}G_{24}$-3') with a *cis*-GG adduct (where G* denotes the location of platinated nucleotides), derived from the NMR structure (PDB code 1A84), containing 767 atoms solvated in a droplet of 1782 TIP3P water molecules (~10 Å thick).

Simulation 2 (Sim2) was for an interstrand cisplatin–DNA decamer derived from the X-ray structure of d(5'-$C_1C_2T_3C_4G_5*C_6T_7C_8T_9C_{10}$-3')•d(5'-$G_{11}A_{12}G_{13}A_{14}G_{15}*C_{16}G_{17}A_{18}G1_9G_{20}$-3') (PDB entry 1A2E),[14] containing 640 atoms solvated in a droplet of 1531 water molecules. Droplet simulations were employed mainly to test the performance of the force field in the

7

'local' region immediately around the Pt center. The AMBER94 force field (in MOE format) and the LFMM parameter file are provided in the Supporting Information (files SF1 and SF2).

For Sim1 and Sim2, the cisplatin/DNA system was frozen and the solvent molecule positions were energy-optimized. With cisplatin/DNA still fixed, the system was then heated to 300 K in two rounds of 10 ps by coupling to a heat bath using the Berendsen algorithm followed by 100 ps simulation to equilibrate the water at a temperature of 300 K maintained by a Nosé–Hoover thermostat. All atoms were then optimized to give the starting point for LFMD simulations followed by 5 ns of production dynamics under NVT conditions. All the atoms were propagated according to Newton's equations of motions with a time step of 2 fs at a mean temperature of 300 K using a Nosé–Hoover thermostat. Bonds involving hydrogen atoms were constrained during the simulations using the SHAKE algorithm.[60] Nonbonded cutoffs (r_1) of 10 Å and an onset (r_0) of 8 Å (the MOE default) were applied to the nonbonded energy terms with the smoothing function:

$$s(r) = \begin{cases} 1 & if \ \ r < r_0 \\ 1 - [x^3(6x^2 - 15x + 10] & if \ \ r_0 \leq r \leq r_1 \\ 0 & if \ \ r > r_0 \end{cases} \tag{2}$$

where $x = \dfrac{r - r_0}{r_1 - r_0}$.

To explore the 'global' structure, periodic boundary conditions are required,[29] and the LFMM method was ported to DL_POLY2.[61] Simulation 3 (Sim3) employed DL_POLY_LF[62] and comprised the interstrand cisplatin–DNA complex from Sim2 now with 3941 water molecules in a periodic box of dimensions 48x45x56 Å.

Finally, simulation 4 (Sim4) comprised an interstrand **P**–DNA dodecamer derived from the X-ray structure of the DNA duplex (PDB entry 3CO3,[63] d(5'-$C_1C_2T_3C_4T_5C_6G_7T_8C_9T_{10}C_{11}C_{12}$-3')• d(5'-$G_{13}G_{14}A_{15}G_{16}A_{17}C_{18}G_{19}A_{20}G_{21}A_{22}G_{23}G_{24}$-3') (Figure 3). This originally contains a monofunctional adduct of *cis*-{Pt(NH$_3$)$_2$(py)}$^{2+}$ with G7. After replacement of the original metal fragment with the **P** fragment, *trans*-{Pt(py)$_2$}$^{2+}$, and formation of the interstrand *trans*-[Pt(py)$_2$(dGua)$_2$]$^{2+}$ cross-link between the N7 positions

8

of the central guanines on the opposite strands of DNA (G7 and G19), the metal and its coordinated groups were optimized with the rest of the residues frozen. The resulting structure which contains 781 atoms solvated with 3400 water molecules in a periodic box of dimensions 45x45x60 Å was then re-optimized via multiple rounds of simulated annealing at 450 K to give the starting point for NPT simulations followed by 6 ns of production with a time step of 2 fs at 300 K and a pressure of 1 atm maintained by Berendsen baro- and thermostats using DL_POLY_LF[61]. Long range interactions were treated by using the Ewald summation method. The SHAKE algorithm was employed to constrain all bonds involving hydrogen atoms in water molecules. A cutoff of 12 Å was applied to the nonbonded interaction. The starting DL_POLY_LF geometry file (CONFIG), parameter file (FIELD) and LFMM file (LFSE.in) are provided in the Supporting Information (files SF3, SF4 and SF5 respectively).
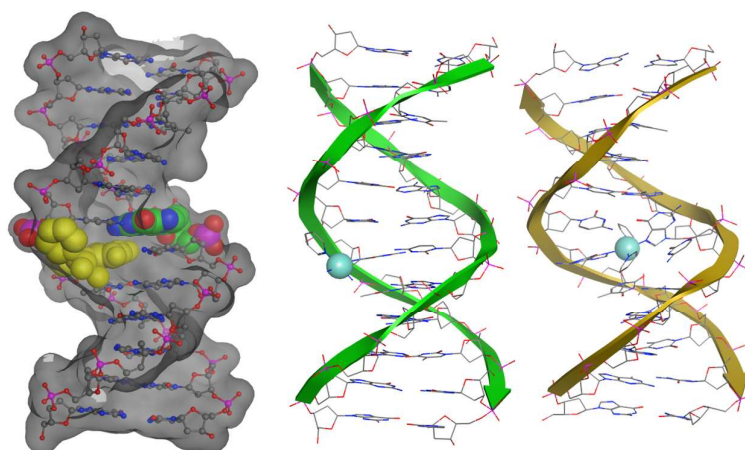

Figure 3: Left and center: X-ray structure of monofunctional adduct between *cis*-{Pt(NH₃)₂py} and DNA (PDB code 3CO3) highlighting the major-groove platination site (yellow) and the position of proposed interstrand crosslink for P-DNA (green carbons on left). Right: initial energy-minimized structure of P-DNA.

Experimental details

Materials

9

A 5 x 10^{-4} M stock solution of **1** was prepared in MilliQ H_2O and stored at 4 °C in the dark. The concentration of platinum in the stock solution was determined by flameless atomic absorption spectrometry (FAAS). The synthetic oligodeoxyribonucleotides were purchased from VBC-Genomics (Vienna, Austria) and purified as described earlier.[64,65] T4 polynucleotide kinase was purchased from New England Biolabs (Beverly, MA, USA), acrylamide, bis(acrylamide), urea and NaCN from Merck KgaA (Darmstadt, Germany), dimethyl sulfate (DMS) from Sigma (Prague, Czech Republic), and [γ-^{32}P]ATP from Amersham (Arlington Heights, IL, USA).

Platination of Oligonucleotides

The duplex containing a single, site-specific interstrand cross-link of **1** was prepared and characterized in the same way as described previously.[64,65] Briefly, the single-stranded oligonucleotide (the top strand of the duplex in Figure 4A) was mixed in stoichiometric amounts with **1**, incubated under irradiation by UVA for 7 min and repurified by HPLC. The oligonucleotide sample was irradiated using the LZC-4V illuminator (photoreactor; Luzchem, Canada) with temperature controller and with UVA tubes (4.3 mW cm^{-2}; λ_{max} 365 nm). Irradiance was measured with a Waldmann PUVA meter, calibrated to the source using a double grating spectroradiometer (Bentham, UK). The platinated (monoadduct containing) top strand was allowed to anneal with unplatinated complementary strand (the bottom strand in Figure 4A) in 0.1 M NaClO$_4$ and incubated for 24 h in the dark at 37 °C. The resulting products were separated on denaturing 8 M urea and 24% polyacrylamide (PAA) gel; the band corresponding to interstrand cross-linked duplex was cut off from the gel, eluted, precipitated by ethanol, and dissolved in Tris.HCl (10 mM, pH 7.4). The cross-linked duplex was analyzed for platinum content by FAAS\z. Additional quantitation of the cross-linked duplex by UV absorption spectrophotometry was used to ascertain that the ratio of platinum adduct per duplex was 1. HPLC purification was carried out using a Waters HPLC system consisting of a Waters 262 pump, Waters 2487 UV detector, and Waters 600S controller with MonoQ HR 5/50 GL column. The FAAS measurements were carried out on a Varian AA240Z Zeeman atomic absorption spectrometer equipped with a GTA 120 graphite tube atomizer. For FAAS analyses, DNA duplex was precipitated with ethanol and dissolved in HCl (0.1 M).
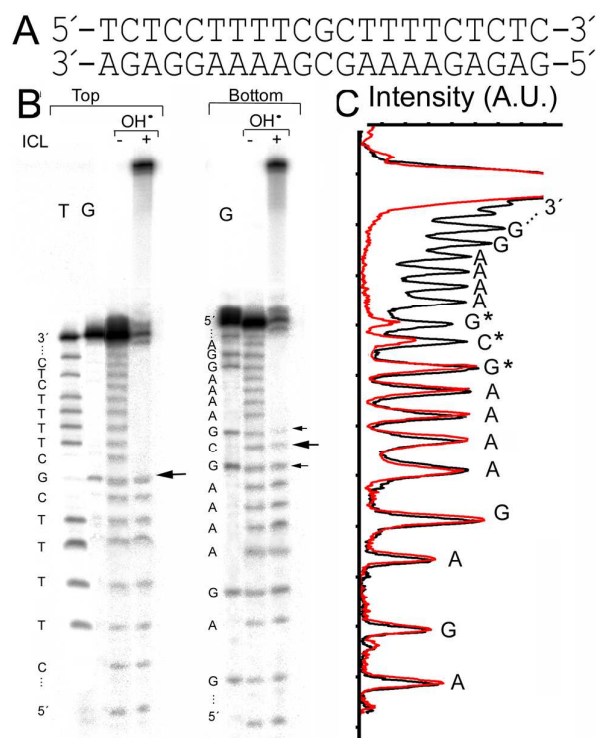
10

Figure 4 Hydroxyl radical footprinting of the interstrand cross-link formed by irradiated FM190 in the duplex CGC. A. Nucleotide sequence of the duplex CGC. B. Shown are autoradiograms of denaturing 24% PAA/8 M urea gel of the products of the reaction between hydroxyl radicals and the duplex CGC either unmodified or containing an interstrand cross link of irradiated 1. The top (left) or bottom (right) strand was 5'-end-labeled. T, G lanes, Maxam-Gilbert-specific reactions for the unplatinated duplex. Arrows indicate the bands that had a lower intensity than the corresponding bands seen for unplatinated duplex. C. Densitograms representing densities of the bands in the right gel (bottom strand was 5'-end labeled) shown in Fig. 1B; black and red lines are the traces for a control sample without interstrand CL and for the interstrand cross-linked duplex, respectively. See the text for other details.

Hydroxyl Radical Footprinting of Interstrand Cross Links

The oligonucleotide duplex containing a single, site-specific intrastrand cross link of **1** was analyzed by hydroxyl radical footprinting as described earlier.[66,67] Platinated (or unplatinated) oligodeoxyribonucleotide duplexes (concentrations 6 nM) that had either the top or bottom strand ^{32}P-labeled at the 5´-end were dissolved in a medium containing 50 mM NaCl and 10

11

mM Tris-HCl (pH 7.5). Cleavage of the phosphodiesteric bonds was achieved by incubating the duplexes in $Fe(NH_4)_2(SO_4)_2$ (0.04 mM), EDTA (0.08 mM), H_2O_2 (0.03%), and sodium ascorbate (2 mM) for 5 min at 20 °C. The reaction was stopped by adding thiourea (15 mM), EDTA (3 mM), sodium acetate (0.3 M), and tRNA (0.3 mg mL^{-1}). After precipitation, the samples were resolved on a 24% denaturing PAA/8 M urea gel, analyzed by autoradiography using the BAS 2500 FUJIFILM bioimaging analyzer, and the radioactivities associated with bands were quantitated with the AIDA image analyzer software (Raytest, Germany). The peak areas corresponding to each band were compared, and when the difference between the control and platinated lanes was more than 10%, the corresponding base was scored as being protected. Maxam-Gilbert sequencing reactions were run in parallel.

Maxam-Gilber (DMS) Footprinting of Interstrand Cross Links

Reaction of the oligonucleotide containing a single, site-specific interstrand cross link of irradiated **1** with DMS was performed as previously described.[65,68-71] The binding sites for platinum in the interstrand cross-linked oligonucleotide were mapped by comparing autoradiograms of fragments obtained from platinated and unplatinated duplexes following modified Maxam-Gilbert sequencing reactions. Base-specific chemical reactions were performed on platinated and unplatinated oligonucleotide that was ^{32}P 5'-end labeled on its top or bottom strand. Aliquots (100 cps) were treated separately in the presence of 1.5 pg of sonicated calf thymus DNA with DMS to give guanine-specific strand-weakening reactions. Reactions were stopped, and the solutions were desalted by precipitation, dried, and treated either with (i) piperidine (1 M, 100 µL, 30 min, 90 °C) or (ii) sodium cyanide (0.4 M, pH 8.4, 30 µL, 15 h, 45 °C) to remove platinum from DNA, followed by desalting and piperidine treatment as in (i). After an alkaline running dye (80% formamide, 10 mM NaOH, xylene cyanol, bromophenol blue) had been added, samples were resolved on a 24 % PAA/8 M urea denaturing gel and analyzed by autoradiography in the same way as the fragments generated by hydroxyl radicals.

Results and discussion

12

Frequent, although not major, adducts formed by bifunctional antitumor analogues of transplatin containing a heterocyclic ligand are interstrand cross links.[66,72] Interestingly, transplatin forms these cross links preferentially between G and complementary C residues,[70] whereas quite surprisingly its analogues, such as *trans*-[PtCl$_2$(NH$_3$)(quinoline)] or *trans*-[PtCl$_2$(NH$_3$)(thiazole)] (*i.e.* the *trans* complexes containing a planar heterocyclic ligand) form these cross links between G residues in the 5'-GC/5'-GC sequences[73] (*i.e.* "cisplatin-like" interstrand cross links[69]). Therefore, it was of interest to identify the residues involved in the interstrand cross link formed by irradiated complex **1**.

Diamminedichloridoplatinum(II) complexes react with DNA in a two-step process.[74] Monofunctional adducts are formed preferentially at N-7 atoms of G residues. These lesions subsequently close to bifunctional cross links (intrastrand and/or interstrand). Considering this fact, we designed the synthetic oligodeoxyribonucleotide duplex CGC (for its sequence see Figure 4A). The pyrimidine-rich top strand of this duplex contains a unique G residue at which the monofunctional adduct of **1** was formed after this strand was mixed with **1** and irradiated. Thus, the choice of the duplex CGC allowed for a cross-linking study under competitive conditions (*i.e.* interstrand cross links were in principle possible between the central G in the top strand and either complementary C or adjacent (flanking) Gs on the opposite strand). The top strand of the duplex CGC containing the monofunctional adduct of irradiated **1** was hybridized with its complementary (bottom), 5'-end ^{32}P-labeled strand. The mixture was incubated at 37 °C in 0.1 M NaClO$_4$, for 24 h in the dark and subjected to gel electrophoresis under denaturing (strand-separating) conditions to separate and quantify the interstrand cross-linked duplexes.

The interstrand cross-linked sample was further analyzed by hydroxyl radical footprinting.[67] The hydroxyl radicals generated by reaction of the EDTA complex of iron(II) with hydrogen peroxide initiate cleavage of the DNA phosphodiester backbone by abstracting a hydrogen atom from a deoxyribose. The hydroxyl radicals cleave mixed-sequence DNA nearly equally at each backbone position.[75] The fragments generated by hydroxyl radicals are then separated on a PAA gel under denaturing conditions.

If this approach is applied to identification of bases involved in the interstrand cross links formed in the duplex CGC by irradiated **1**, then the fragments corresponding to all bases in

13

the bottom strand from the 5'-end up to the bases involved in interstrand cross links should migrate in the gel just as those of the unplatinated duplex. On the other hand, fragments corresponding to the bases behind the cross link in the 3' direction should migrate with a markedly slower mobility because the generated fragments are cross-linked to the complementary strand.

The cleavage patterns for the platinated and unplatinated oligonucleotides, as well as the Maxam-Gilbert sequencing patterns for the unplatinated oligonucleotide, are shown in Figure 4B. For the two strands of the unplatinated duplex CGC, a uniform cleavage was obtained. For the platinated duplex in which the bottom strand only was 5'-end-labeled with ^{32}P, the last fragment migrating in the same way as that due to the cleavage of the unplatinated duplex, corresponded to the 3' G adjacent to the C complementary to the platinated G in the top strand. However, the intensity of this band was lower in comparison with the band corresponding to the same base in the unplatinated bottom strand.

A plausible explanation for this observation is that only a part of the molecules of the duplex CGC contained the interstrand cross link involving this 3'G and that the remaining platinated duplexes contained the interstrand cross link involving the adjacent base in the 5' direction, i.e. single C (complementary to the platinated G in the top strand). But also the intensity of this band was lower in comparison with the band corresponding to the same base in the unplatinated bottom strand.

Thus, as deduced above, the sample of the duplex CGC interstrand cross-linked by irradiated **1** had to contain another fraction of duplexes containing the interstrand cross link involving the adjacent base in the 5' direction, which is 5'G. Intensities of the bands corresponding to the latter base and all other bases in the 5' direction were not attenuated in comparison with the bands corresponding to the same bases in the unplatinated bottom strand. Thus, it is reasonable to conclude that interstrand cross links other than those involving G in the top strand of the duplex CGC and complementary C or either of flanking Gs were not formed by irradiated **1**.

Hydroxyl radical footprinting only provided qualitative information about base residues involved in the interstrand cross link. Therefore, to obtain information about proportional

14

representation of individual types of the interstrand cross links of irradiated **1**, duplex CGC interstrand cross-linked by irradiated **1** was further analyzed by DMS footprinting. In this assay, platinated and unmodified strands (5'-end-labeled with ^{32}P) are reacted with DMS which methylates the N7 position of guanine residues in DNA, producing alkali labile sites.[76] However, if N7 is coordinatively bound to platinum, it cannot be methylated. The oligonucleotides are then treated with hot piperidine and analyzed by denaturing PAA gel electrophoresis. For the unmodified oligonucleotides, shortened fragments due to the cleavage of the strand at the methylated guanine residues are observed in the gel. However, no such bands are detected for the platinated guanine residues.

The sample of duplex CGC interstrand cross-linked by irradiated **1** in which the top strand was only 5'-end-labeled with ^{32}P was reacted with DMS which does not react with platinated G residues because N7 is no longer accessible.[65,68,70,71] The adducts were removed by NaCN,[68,69] and then the sample was treated with piperidine. In the unplatinated duplex, the central G residue in the top strand was reactive towards DMS (Figure 5A, left panel) whereas it was no longer reactive in the cross-linked duplex. This observation confirms that the unique G residue in the top strand remained platinated and was involved in the interstrand cross link contained in the single fraction of interstrand cross-linked duplex.[65,68,70,71]

In additional studies, the interstrand cross-linked duplex CGC in which the bottom strand was 5'-end labeled with ^{32}P was examined (Figure 5A, right panel). After the interstrand cross-linked duplex was reacted with DMS, the samples were then further treated with NaCN to remove the adducts and finally also with piperidine. The treatment with piperidine of the control unplatinated duplex resulted in cleavage at all G sites in the bottom strand (Figure 5A, left panel). When the cross-linked duplex treated with DMS and subsequently NaCN was cleaved, bands corresponding to all G residues in the bottom strand were observed that had the same intensity as the corresponding bands seen for unplatinated duplex, except for the G residues flanking single C (complementary to the platinated G in the top strand) (Figure 5B). As shown in Figure 5B, the intensities of these bands were approximately 80% of the intensities observed for the corresponding bands seen for the unplatinated duplex (the means calculated from three independent experiments for band corresponding to 3' G and 5´G were 79% and 81% , respectively; the standard deviations were 2% and 3%, respectively). This

15

result, along with the results of hydroxyl radical footprinting (Figure 4B,C), can be interpreted to mean that irradiated **1** forms three types of the interstrand cross links, ~20% of these cross links are those between Gs in the 5'-GC/5'-GC sequence, ~20% between Gs in the 5'-CG/5'-CG sequence and remaining ~60% between G and complementary C.
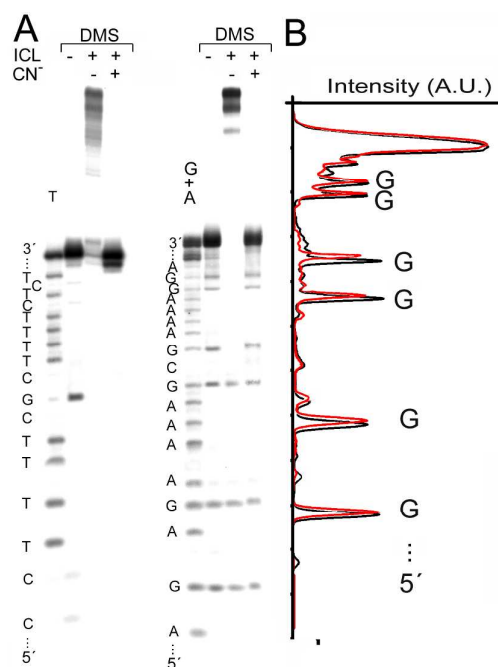

Figure 5 Dimethyl sulfate (DMS) footprinting of the interstrand cross-link formed by irradiated 1 in the duplex CGC. A. Shown are autoradiograms of denaturing 24% PAA/8 M urea gel of the products of the reaction between DMS and the duplex CGC either unmodified or containing an interstrand cross link of irradiated 1. The top (left) or bottom (right) strand was 5'-end-labeled. T, G+A lanes, Maxam-Gilbert-specific reactions for the unplatinated duplex. B. Densitograms representing densities of the bands in the right gel (bottom strand was 5'-end labeled) shown in Figure 5A; black and red lines are the traces for a control sample without interstrand cross link **treated with DMS and for the interstrand cross-linked duplex treated with DMS and subsequently NaCN, respectively. See the text for other details.**

Having established the possibility of interstrand G-G crosslinks involving *trans*-{Pt(py)$_2$}, we set about modeling studies to obtain atomistic detail. Rather than employ the sequence used for the experimental studies, which is of unknown structure, we chose instead to base our studies on a known system which already had an analogous Pt complex bound, albeit in a

16

monofunctional manner. However, prior to this, we had first to construct and validate a suitable LFMM force field.

Partial charges for coordinated guanines were derived by adding the change in CHelpG partial atomic charges between isolated and Pt-coordinated guanine to the standard MMFF94[53-57] or AMBER94[77] FF partial charges for uncoordinated guanines. Figure 6 displays the complex, *cis*-[Pt(NH$_3$)$_2$Cl(dGuo)]$^+$, used for developing the new LFMM/MMFF94 and LFMM/AMBER94 charge scheme (Figure 7, with further details in Table S1 of the Supporting Information). The charge on Pt, q_{Pt}, can be computed from the total charge transferred by all the ligands to Pt(II) , ΔQ:
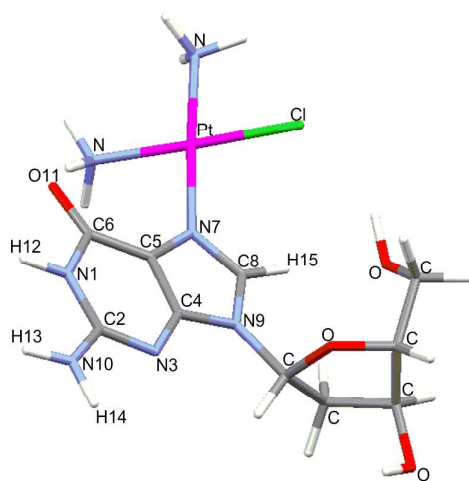
$$q_{Pt} = 2 - \Delta Q \qquad (3)$$

Figure 6: Model compound, *cis*-[Pt(NH$_3$)$_2$Cl(dGua)]$^+$, used to derive the new charge scheme for Pt-binding guanines.
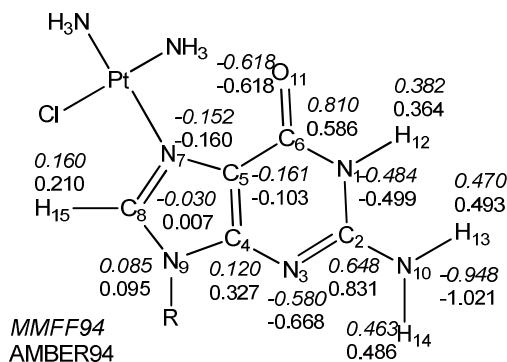
17

Figure 7: New LFMM/MMFF94 and LFMM/AMBER94 charge schemes for N7-platinated deoxyguanosine (dGua(Pt)), derived from CHelpG charges of the model compound, *cis-*[Pt(NH₃)₂Cl(dGua)]⁺, in Figure 6.

Having fixed the partial charge scheme, LFMM requires Morse function parameters for Pt–L bond stretching (D, r_0 and α), and ligand–ligand repulsion parameters (A_{LL}) for L-Pt-L angle bending. The Cambridge Structure Database[78] (CSD) was searched for X-ray structures of complexes that could be used to optimize new Pt-guanine parameters. Fifteen structures were selected and, in conjunction with the existing LFMM parameters for Pt-NH₃ and Pt-Cl,[38] Pt-guanine parameters were manually optimized to reproduce experimentally observed structures with a target deviation in all Pt–L bond lengths of less than 0.05 Å and G–Pt–G bond angles of less than 3°. Overlays of the LFMM and X-ray structures are depicted in Figure 8 and the Pt-L distances are given in the Supporting Information (Table S2).
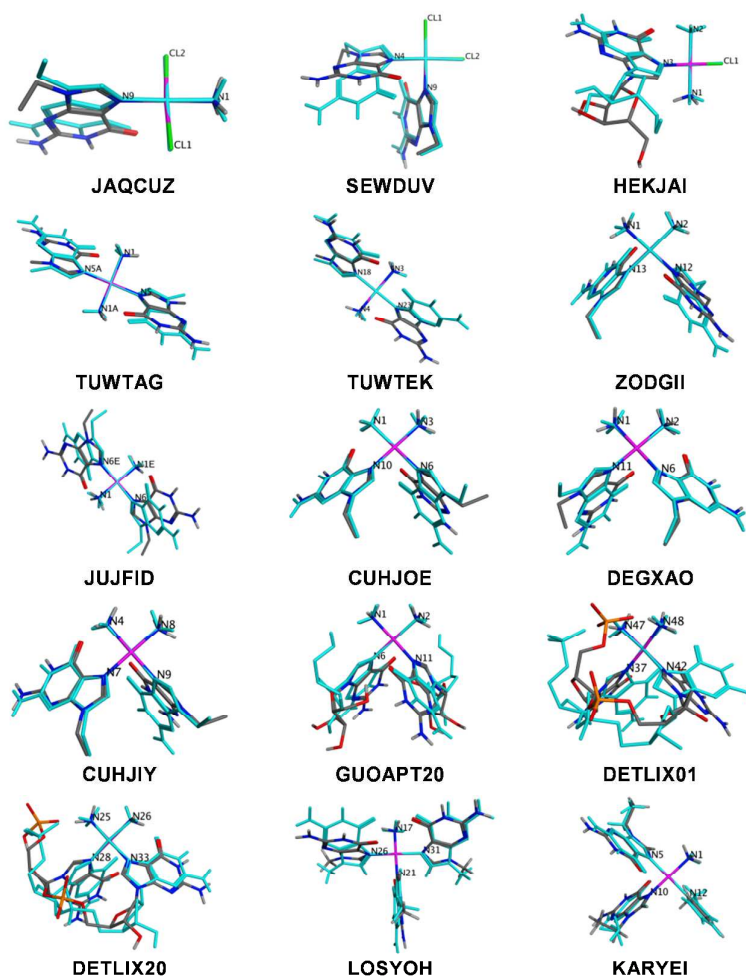
18

Figure 8: Overlays of energy-minimized LFMM (colored by element) and X-ray (cyan) structures with CSD refcodes.

Apart from *cis*-diammine-bis(9-ethylguanine)-platinum(II) (DEGXAO) where LFMM places one of the ammine ligands 0.075 Å further from the metal than observed experimentally, reproducing the PtL$_4$ structure accurately is relatively straightforward. The planar geometry is a function of the low-spin d^8 configuration and arises naturally and automatically from the LFSE inherent in LFMM.[31] However, an equally, if not more, significant feature to consider is the local geometry around guanine N7, in particular, by how much the metal is displaced from the ligand plane.

19

Most of the complexes in Figure 8 do not explore this feature very well since the κ^1 binding mode makes it easy for the Pt to lie in the guanine plane. The one that does – the $\kappa^2 N$ diammine-(deoxy-guanylyl-guanylyl-N7,N7')-platinum(II) (DETLIX) – has some problems. There are the five separate CSD entries for DETLIX some of which show disorder. The two examples included in Figure 8, DETLIX01[79] and DETLIX20[80], show fairly large variations of what should be the same bonds (Table S1). We conclude that the differences between LFMM and experiment may be attributable to the quality of the experimental data. Thus, we turn to theoretical studies to validate the FF further.

Firstly, the vibrations of *cis*-[Pt(NH$_3$)$_2$(Cl)(dGuo)]$^+$ (Figure 6) calculated using LFMM and DFT/BP86 were compared. The computed values of the low energy frequencies are similar (Table S3 in Supporting Information) and while the detailed atomic motions vary somewhat, the comparable energies, and hence force constants, suggest that the LFMD trajectories should be realistic. Secondly, the energy required to bend a model guanine system, [Pt(MeGuanine)(terpy)]$^{2+}$ (terpy = 2,2',2''-terpyridine, Figure 9) was calculated.
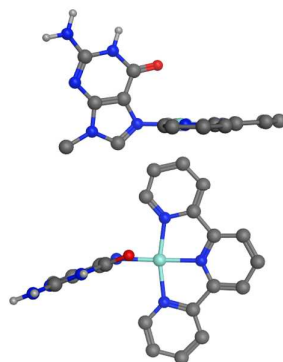

Figure 9: Perpendicular views of the model system to assess the energetics of guanine bending. The guanine is shown bent 20 ° off its minimum-energy position. (Non-polar hydrogens are not shown.)

The minimum-energy structure places the Pt in the ligand plane. Bending the guanine 20 ° off the Pt-N axis (Figure 9, bottom) raises the DFT energy by 6.5 kcal mol^{-1} versus 8.8 kcal mol^{-1} for MMFF94 and 7.8 kcal mol^{-1} for AMBER94. Thus, the FFs are a little 'stiffer' than DFT but not drastically. Finally, further comparisons were made between LFMM results and previously reported QM/MM data.

20

Gkionis and Platts[81] employ the ONIOM method with the quantum part comprising Becke's half-and-half functional, 6-31+G** basis sets on the light atoms and the Stuttgart–Dresden SDD ECP/basis on platinum, with the AMBER FF as the MM part. As expected, for the PtL_4 moiety LFMM bond lengths and bond angles accurately reproduce QM/MM. The largest absolute difference between LFMM and QM/MM Pt-L contacts is 0.03 Å with the average error ~0.02 Å. (Table S4 in Supporting Information). However, the bending at the N7 positions is less for LFMM than for QM/MM. For single strand model systems (Figure 10, left) the overall agreement remains reasonably good but for double stranded systems (Figure 10, right), where the bending strain is higher, the spacing between the base planes is increased.

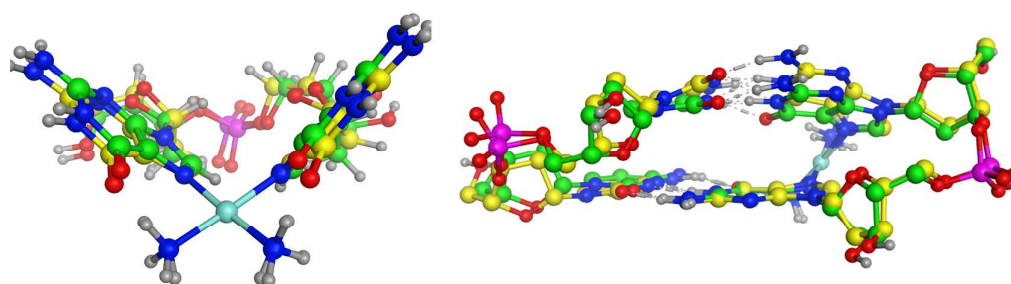**Figure 10: Overlay of QM/MM (green carbons) and LFMM (yellow carbons) for single strand (left) and double-strand (right) GpG model system.**

However, while the LFMM certainly gives 'flatter' Pt-guanine coordination, there remain examples with significant distortions (Figure 11). Hence, the current approach appears capable in principle of accommodating the necessary geometrical variations.
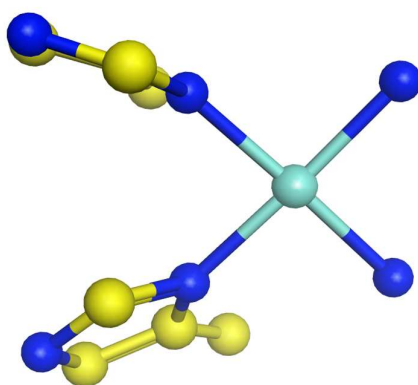

21

Figure 11: Detail of LFMM N7 coordination for double-stranded model of Figure 10.

The parameter development described thus far mostly employed the MMFF94 force field since it has a richer set of ligand types. However, for DNA simulations, we wish to use an AMBER force field. Transferring LFMM parameters from MMFF94 to AMBER94 is straightforward, as shown previously,[82] and involves only some minor adjustments of the partial charges (see Figure 7) and renaming of the atom types.

Droplet LFMD Simulations of the 1,2-intrastrand and interstrand cisplatin–DNA Complexes.

The DommiMOE simulation of the 1,2–intrastrand cisplatin–DNA adduct started from the NMR dodecamer structure (PDB code 1A84) to which counterions and water molecules were added as described above. The potential energy converges after ~2.5 ns (Figure S1). Thus, the first 2.5 ns of the trajectory were excluded, while the remaining 2.5 ns were used in computing the average structure, distances, and angles. A comparison between LFMD, previous QM/MM results[83] and experimental data is given in Table 1. These include three root-mean-square deviations (RMSDs) for, respectively, Pt–L bond lengths, the heavy (non-hydrogen) atoms of Pt(II) and its ligands NH_3 and Gua, and of the entire Pt-DNA system. Figure 12 displays an overlay of the LFMD and experimental structure. As expected, the local geometry around the Pt center is well reproduced. The DommiMOE LFMD RMSDs for Pt–L bond lengths, heavy atoms of cisplatin–guanine, and of the cisplatin–DNA complex are 0.041, 0.554, and 0.917 Å, respectively. The QM/MM simulations for the same adduct have RMSDs of 0.04, 1.50 and 4.20 Å.[83]
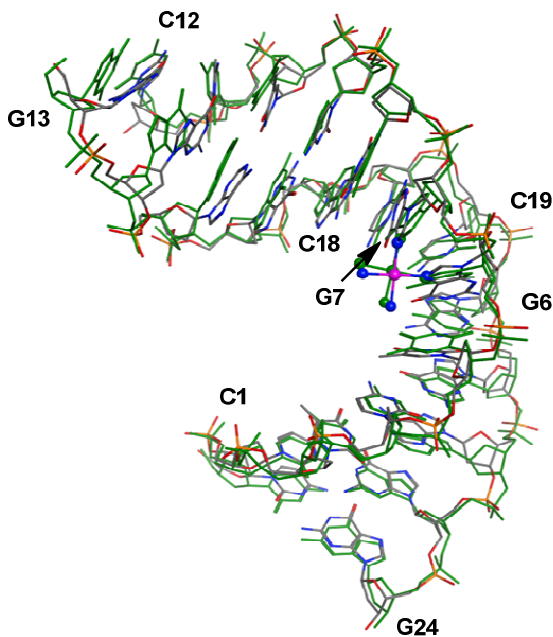
22

Figure 12: NMR structure (green) of the 1,2-intrastrand Cisplatin–DNA Complex: PDB 1A84 with the sequence d(5'-C$_1$C$_2$T$_3$C$_4$T$_5$G$_6$*G$_7$*T$_8$C$_9$T$_{10}$C$_{11}$C$_{12}$-3')•d(5'-G$_{13}$G$_{14}$A$_{15}$G$_{16}$A$_{17}$C$_{18}$C$_{19}$A$_{20}$G$_{21}$A$_{22}$G$_{23}$G$_{24}$-3') where the -G$_6$* G$_7$*- site has been modified by cisplatin, superimposed upon the averaged droplet-simulation LFMD structure (colored by element; Pt^{2+} in magenta). Pt^{2+} and its directly bounded atoms are displayed in ball and stick mode.

Table 1: Comparison between Selected LFMD, QM/MM,[83] and Experimental Pt Bond Distances and Angles and atomic RMSDs for 1,2-intrastrand Cisplatin–DNA Complex PDB 1A84

Method	N7–Pt–N7 (deg)	Pt–N (Å)	Pt–N' (Å)	Pt–N7 (Å)	Pt–N7' (Å)	RMSDs[a] (Å)
NMR	90.1	2.049	2.050	2.046	2.051	
QM/MM	86	2.11	2.09	2.06	2.03	0.04 /1.50 /4.20
DommiMOE	88.9	2.022	2.024	1.986	2.011	0.041/0.554/0.917

[a]RMSDs for Pt–L bond lengths, heavy atoms of {Pt(NH$_3$)$_2$(Gua)$_2$}$^{2+}$ and heavy atoms of whole cisplatin–DNA complex

The droplet simulation of the 1,2–interstrand cisplatin–DNA adduct started from the X-ray structure (PDB code 1A2E). Again, a reasonable degree of the potential energy convergence

23

was obtained after ~2.5 ns (Figure S2), and therefore the average structure was generated using the last 2.5 ns of a 5 ns simulation. As shown in Table 2, the droplet LFMD local geometry around the metal agrees well with experiment.
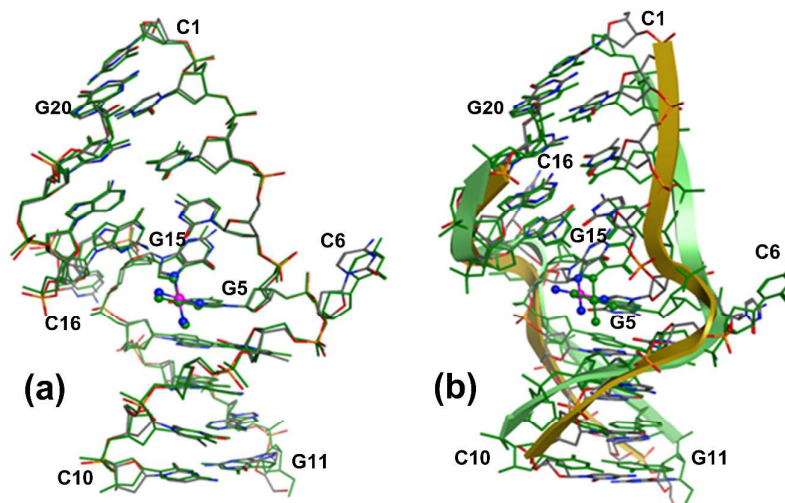

Figure 13: Crystal structure (green) of the cisplatin–DNA complex PDB 1A2E with the sequence d(5'-$C_1C_2T_3C_4G_5$*$C_6T_7C_8T_9C_{10}$-3')• d(5'-$G_{11}A_{12}G_{13}A_{14}G_{15}$*$C_{16}G_{17}A_{18}G1_9G_{20}$-3'), where G* denotes the location of platinated nucleotides, superimposed upon the average LFMD structure (colored by element; Pt^{2+} in magenta) derived from simulations with (a) a solute molecule inside a 'drop' of solvent and with (b) periodic boundary conditions. Pt^{2+} and its directly bounded atoms are displayed in ball and stick mode.

The droplet protocol is good for examining the structure in the immediate vicinity of metal centers.[84] The use of a Morse potential to describe the 'conventional' force field contribution to M-L bonding allows, in principle, for the M-L bond to effectively dissociate.[85] Hence, if our treatment of the Pt lesions is grossly incorrect, we would anticipate computing anomalously long Pt-L contacts. However, the droplet method introduces a surface effect which tends to restrain the 'global' geometry. Such surface effects can be alleviated using periodic boundary conditions and hence the same interstrand cisplatin–DNA complex was simulated with periodic boundary conditions using our LFMM implementation in DL_POLY (Figure S3, Supporting Information). The RMSD for Pt–L bond lengths, the $\{Pt(NH_3)_2(dGua)_2\}^{2+}$ fragment and overall heavy atoms certainly increase to 0.044, 0.823, and 2.488 Å, respectively, while the overlay of computed and X-ray structures (Figure 13,

24

right) highlights the movement of the backbone during the simulation. Compared to the periodic boundary DL_POLY_LF simulation, the solvent droplet LFMD simulation is 'stiffer'. To try to assess just how big the surface effects might be, we removed the *cis*-$\{Pt(NH_3)_2\}^{2+}$ fragment and carried out a further 6 ns droplet LFMD simulation to see whether the DNA would straighten out. The global bending angle does decrease from 47.2° to 24°, but the distorted duplex is unable to return to a B-DNA conformation on this time scale since one of the bases has rotated out of alignment with its complementary base (Figure S4, Supporting Information).

Table 2: Comparison between Selected LFMD and Experimental Pt Bond Distances and Angles and RMSD of Geometrical Data for Interstrand Cisplatin–DNA Complex PDB 1A2E

Method	N7–Pt–N7	Pt–N	Pt–N'	Pt–N7	Pt–N7'	RMSD[a]
	(deg)	(Å)	(Å)	(Å)	(Å)	(Å)
X-ray	86.8	2.010	1.997	2.000	1.999	
DommiMOE	87.9	2.033	2.037	2.000	2.001	0.023/0.265/0.494
DL_POLY_LF	90.2	1.963	1.966	1.953	1.950	0.044/0.823/2.488

[a]RMSDs for Pt–L bond lengths, heavy atoms of $\{Pt(NH_3)_2(Gua)_2\}^{2+}$ and heavy atoms of whole cisplatin–DNA complex

Periodic Boundary LFMD Simulation of the Interstrand P–DNA Complex

The simulation of the interstrand **P**–DNA complex (DL_POLY_LF with periodic boundary conditions) started from the modified X-ray structure (PDB entry 3CO3) as described above. Analysis of the α and γ backbone torsion angles (see Figure S4, Supporting Information) shows little variation apart from those for C6 which display g^+ to t transitions and α for A15 which changes from g^+ to g^- after about 4 ns. The average structure generated from the last 2 ns of a 6 ns simulation is displayed in Figure 14a and an expanded view of the platinum-binding site is shown in Figure 14b. The binding of the *trans*-$\{Pt(py)_2\}$ fragment completely disrupts the hydrogen bonding between C6 and G19 such that the former becomes much more solvent exposed (*vide infra*) which accounts for the α/γ variations.

25

A more detailed analysis of the local and global structural parameters for nucleic acids can be generated using the program Curves+.[86] The results for the DL_POLY_LF simulations of 1A2E and **P**-DNA are presented in Figure 15.
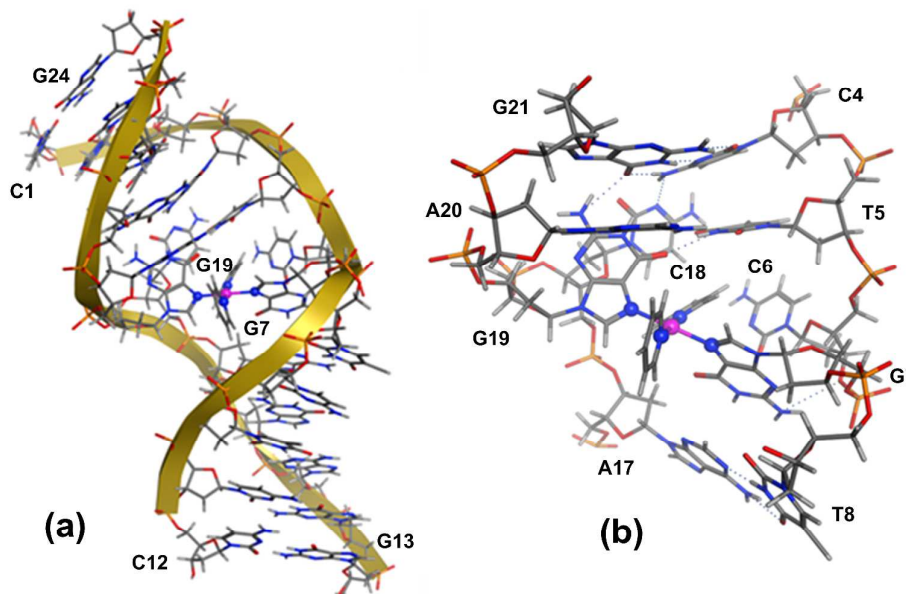

Figure 14: The average LFMD structure derived from simulations of interstrand P–DNA complex, an interstrand crosslink on the DNA duplex with the sequence d(5'-$C_1C_2T_3C_4T_5C_6G_7$*$T_8C_9T_{10}C_{11}C_{12}$-3')•d(5'-$G_{13}G_{14}A_{15}G_{16}A_{17}C_{18}G_{19}$*$A_{20}G_{21}A_{22}G_{23}G_{24}$-3') containing the *trans*-{Pt(py)$_2$}$^{2+}$ fragment coordinated to G_7 and G_{19}, with periodic boundary conditions. (a) The P–DNA complex. (b) An expanded view of the platinum-binding site. Pt^{2+} and its directly bounded atoms are displayed in ball and stick mode.

Coordination of the *trans*-platinum fragment *trans*-{Pt(py)$_2$}$^{2+}$ to G7 and G19 causes disruption of the T5-A20, C6-G19*, and G7*-C18 base pairs and a propeller twist of the platinated central base pairs by ~120°, resulting in the formation of hydrogen bonds between G19 NH2 and G21 O6, G19 O6 and A20 NH6, G21 O6 and T5 NH3, and G7 NH2 and 3' oxygen of the sugar moiety 6. On the other hand, C6 and C18 are more solvent-exposed than in B-DNA, a feature similar to that found in the X-ray structure of the interstrand cross-link, PDB 1A2E (Figure 14b). The local distortions lead to a global bend of the duplex of ~67° and

26

a helix unwinding of ~20°. The larger RMSD of the $\{Pt(NH_3)_2(dGua)_2\}^{2+}$ moiety from those in the starting structure, as compared to the RMSD of the heavy atoms for the rest of the complex, indicates a metal-binding site which is less rigid than the rest of the DNA.

Figure 15 summarizes the minor groove width (Min-W) and depth (Min-D), the C5' -C4' -C3' -O3' (δ) torsion angles, and the local inter-base pair parameters: rise, tilt, and twist for the two interstrand platinated duplexes in this work. Unlike the wide and shallow features on either side of the platination site in cisplatin–DNA complexes, the minor groove in **P**–DNA complex is wide and shallow on one side and narrow and deep on the other. Sugar puckers can be inferred from the δ torsion angles. Such an analysis as that of Figure 15c shows that the **P**–DNA complex displays a more A-DNA-like C3'-endo conformation at the platinated site compared to the structure of 1A2E. The asymmetric helix unwinding on the two strands of the **P**–DNA complex is related to the decreasing inter-base twist angles at the metal-binding site (Figure 15d).
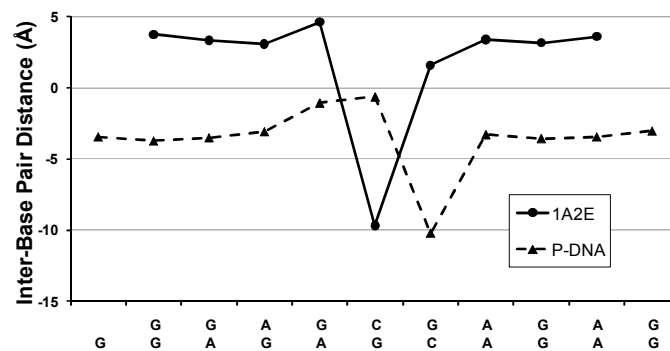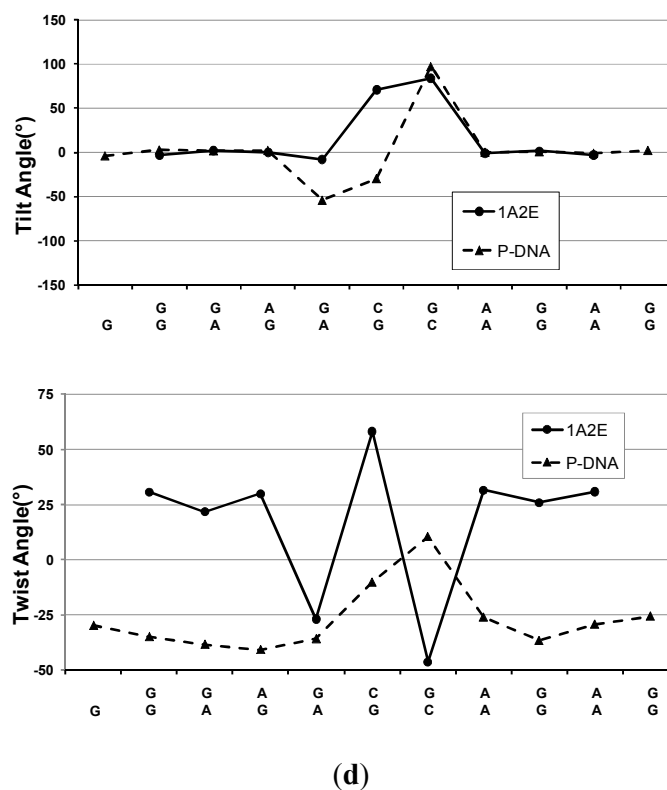

(a)

(**b**)

(**c**)

28

(d)
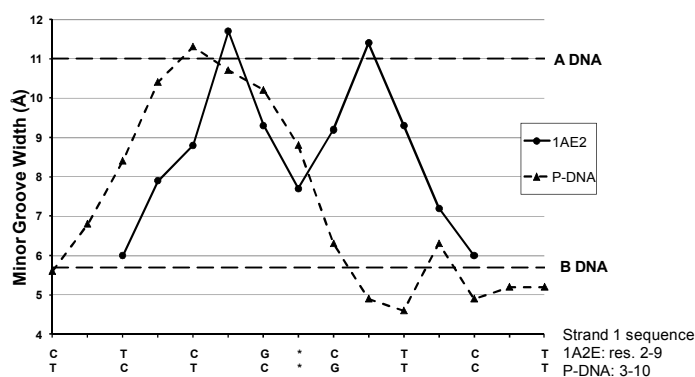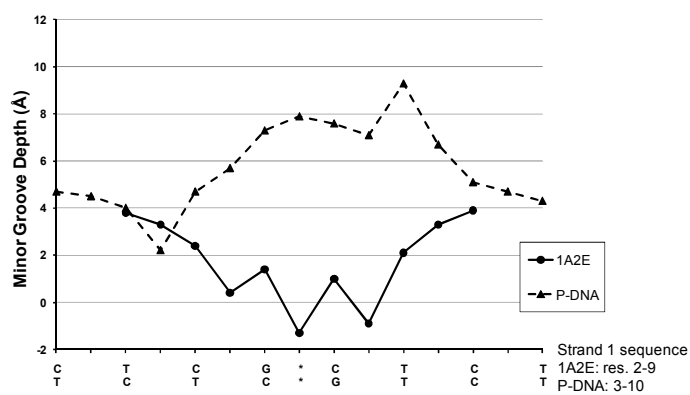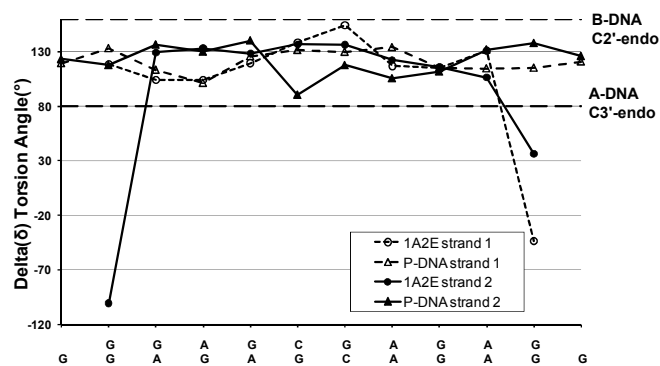
Figure 15: Graphical representation of base pair parameters from Curves+ analysis as a function of base pair for the two of interstrand platinated duplexes. Sequences are presented from residue 2 to 9 and residue 3 to 10 in strand 1 for 1A2E and P-DNA complex, respectively, to provide an illustrative comparison between structures with different DNA sequences in (a) and (b); whereas the complementary sequences are presented from residue 20 to 11 and residue 24 to 13 in strand 2 for 1A2E and P-DNA complex, respectively in (c) and (d).

In the X-ray structure of the mono-functionalized {Pt(NH$_3$)$_2$py} adduct used as the starting point from which a **P**-DNA model was constructed (PDB 3CO3), the Pt(II) complex binds in the major groove of DNA. However, in our simulation of the **P**-DNA complex, the platinum group which cross-links the interstrand guanine bases via their N7 positions protrudes into the minor groove of the DNA duplex, and these N7 atoms located initially in the major groove are now also in the minor groove. The simulations therefore predict for **P**-DNA that platinum compaction in the minor groove leads to a bend toward the minor groove as in the X-ray structure of the interstrand crosslink, 1A2E.

29

While this prediction awaits definitive experimental verification, we believe that starting with a system as close to our target as possible and then using dynamics, as apposed to simple energy minimization as was done for the first cis-platin-DNA simulations, is a better way of exploring the potential energy surface in order to generate suitable models. Further extensions of this work would be to construct LFMM parameters for Pt-cytosine binding and to explore other possible inter and intra-strand binding modes.

Conclusions

In this work, we have extended the LFMM parameters for Pt(II) to allow simulations involving the metal bound to the N7 position of guanines in DNA. LFMM provides a relatively sophisticated description of metal-ligand bonding which captures most of the essential physics around the metal center. For low-spin d^8 Pt(II) systems such as those studied here, the square-planar geometry of the platinum fragment is generated automatically. Also, the computational efficiency of LFMM allows relatively extensive molecular dynamics simulations from which a detailed description of global DNA parameters can be extracted. Compared to QM/MM, LFMD appears to afford closely comparable accuracy, but around four orders of magnitude faster.[36]

Inevitably, how well platinum–DNA complexes can be modeled is based on the interplay between LFMM for the metal center and conventional MM for the 'organic' parts. Our choice to use AMBER94 in this work is partly based on its performance and partly dictated by what is available in the MOE package. We acknowledge that more recent force fields are available and that these might describe some of the more intricate structural parameters of DNA better. However, our experience with the LFMM versions of AMBER94 and MMFF94 suggest that the structure in the vicinity of the transition metal binding is quite similar despite the quite different forms of the functions in each force field energy expression so we believe our conclusions would not be significantly altered by using a different force field.

Given the observed formation of *trans*-[Pt^{II}(py)$_2$(5'-GMP)$_2$]$^{2+}$ upon irradiation of the anticancer prodrug *trans,trans,trans*-[Pt(N$_3$)$_2$(OH)$_2$(pyridine)$_2$], we undertook extensive experimental studies to establish that *trans*-{Pt(py)$_2$} does form GG interstrand DNA crosslinks. These were both 5'-CG/5'-CG crosslinks and 5'-GC/5'-GC crosslinks, as well as

30

crosslinks between G and the complementary C. We then explored a possible GG crosslinked system derived from the experimentally characterized mono-functional adduct involving *cis*-$\{Pt(NH_3)_2(py)\}$.

The most interesting features of the structural deviations in DNA induced by platination are the global bend of the double helix and the deformation of the minor groove. Inspection of the overall helix bend angle and the variation in minor groove width using the program Curves+[86] reveals the average LFMD structure of **P**-DNA exhibits more bending (67°) and less unwinding (20°) than an interstrand cisplatin–DNA adduct (bent by 60° and unwound by 81°) as well as less bending than a reported transplatin interstrand cross-link (bent by 26° and unwound by 12°).[39] The **P**-DNA simulations further suggest that Pt binding induces a bend towards the minor groove which is also observed in the X-ray structure of the cisplatin interstrand crosslink (PDB code 1A2E) but contrasts with the major groove binding motif of the monofunctional adduct used as the basis for building a **P**-DNA model. Overall, the proposed photoadduct bears a closer resemblance to the intrastrand cisplatin–DNA adduct, PDB 1A84, (bent by 83.2° and unwound by 36°) which is of potential importance in the molecular mechanism of action of this photoactivatable complex.

A quantitative analysis of the influence of nucleosomal core proteins on specific drug–DNA interactions using a *Taq* DNA polymerase stop assay has revealed that larger platinum compounds generally display a greater tendency to target the linker region of the nucleosomal DNA and have less access to nucleosomal core DNA.[28] For example, dichloro(N-[3-[(2-aminoethyl)amino]propyl]-9-aminoacridine-4-carboxamide)platinum(II) with a molecular weight of 603 produces a higher average linker-core ratio (L/C ratio) of 2.52 compared to cisplatin (molecular weight of 300, L/C ratio of 1.32). Upon binding to the linker region of the nucleosomal DNA, the platinum modification could (i) enhance the binding of histone H1 and the high mobility group (HMG1) protein[87] and shield the damage site from recognition by DNA repair machinery[11,39,87] by having a dramatic effect on the global curvature of the DNA similar to a cisplatin 1,2-intrastrand lesion, increasing the flexibility of the helix at the local site of the interstrand cross-link, (ii) attenuate the negative electrostatic potential of backbone phosphates by widening the minor groove at one end of the platinated site, and (iii) change the groove landscape by deepening the minor groove at the opposite end of the

31

platinated site together with A-DNA-like conformations and the above structural factors, and thus affect the formation of base-specific hydrogen bonds in the major groove and the electrostatic potential in the minor groove, two general mechanisms for protein–DNA recognition.[88] The compound can also access nucleosomal core DNA. With a striking similarity to the global shape of the intrastrand cis-$\{Pt(NH_3)_2\}^{2+}$ 1,2-d(GpG) cross-link, the $trans$ interstrand **P**–DNA adduct may influence the rotational and translational positioning of DNA in nucleosomes.[26]

Acknowledgments

Supporting Information Available:

Reference 40 in full. Further computational details. Table S1: LFMM/MMFF94 and LFMM/AMBER94 charge schemes for dGua(Pt) derived from CHelpG charges of cis-$[Pt(NH_3)_2Cl(dGua)]^+$. Table S2: Comparison of LFMM-optimized and Experimental Pt–L Bond Lengths (in Å) for Pt^{2+} Complexes containing Guanine. Table S3: The computed lower energy LFMM and QM frequencies (cm^{-1}) for cis-$[Pt(NH_3)_2Cl(dGua)]^+$ in Figure 3 listed in energy order (i.e. the nature of individual frequencies are not necessarily the same). Table S4: LFMM-Optimized and QM/MM M–L Bond Lengths (in Å) for double-stranded Pt complexes. Figure S1: The potential energy U(r) of 1A84 at time t in kcal/mol during LFMD simulations using DommiMOE. Figure S2: The potential energy U(r) of 1A2E at time t in kcal/mol during LFMD simulations using DommiMOE. Figure S3: The simulation box used

32

for DL_POLY calculations on P-DNA complex. Figure S4: α/γ angles for the last 500ps of the P-DNA simulation. Figure S5: The average LFMD structure derived from simulations of deplatinated 1A2E with periodic boundary conditions. Coordinates 1: Averaged 1A2E coordinates from DL_POLY simulation in PDB format. Hydrogens and counterions stripped. Coordinates 2: Averaged P-DNA coordinates from DL_POLY simulation in PDB format. Hydrogens and counterions stripped. File SF1: koll94_tm.ff file. MOE AMBER94 parameters for DommiMOE simulations. File SF2: LFMM_AMBER94.par file. LFMM parameters for DommiMOE simulations. File SF3: P-DNA CONFIG file for DL_POLY_LF simulation exported from MOE. File SF4: P-DNA FIELD file for DL_POLY_LF simulations exported from MOE. File SF4: Additional LFMM file for DL_POLY_LF P-DNA simulations - LFSE.in. This material is available free of charge via the Internet at http://pubs.acs.org.

References:

(1)   Wong, E.; Giandomenico, C. *Chem. Rev.* **1999**, *99*, 2451.

(2)   Kelland, L. *Nat. Rev. Cancer* **2007**, *7*, 573.

(3)   Blindauer, C. A.; Harvey, I.; Bunyan, K. E.; Stewart, A. J.; Sleep, D.; Harrison, D. J.; Berezenko, S.; Sadler, P. J. *J. Biol. Chem.* **2009**, *284*, 23116.

(4)   Deubel, D. V.; Lau, J. K. C. *Chem. Commun.* **2006**, 2451.

(5)   Reedijk, J. *Platinum Met. Rev.* **2008**, *52*, 2.

(6)   Jamieson, E. R.; Lippard, S. J. *Chem. Rev.* **1999**, *99*, 2467.

(7)   Baik, M. H.; Friesner, R. A.; Lippard, S. J. *J. Am. Chem. Soc.* **2003**, *125*, 14082.

(8)   Mantri, Y.; Lippard, S. J.; Baik, M. H. *J. Am. Chem. Soc.* **2007**, *129*, 5023.

(9)   Deubel, D. V. *J. Am. Chem. Soc.* **2006**, *128*, 1654.

(10)   Reedijk, J. *Chem. Rev.* **1999**, *99*, 2499.

(11)   Jung, Y.; Lippard, S. J. *Chem. Rev.* **2007**, *107*, 1387.

(12)   Fuertes, M.; Alonso, C.; Perez, J. *Chem. Rev.* **2003**, *103*, 645.

(13)   Bradley, L. J. N.; Yarema, K. J.; Lippard, S. J.; Essigmann, J. M. *Biochemistry* **1993**, *32*, 982.

(14)   Coste, F.; Malinge, J.; Serre, L.; Shepard, W.; Roth, M.; Leng, M.; Zelwer, C. *Nucleic Acids Res.* **1999**, *27*, 1837.

(15)   Gelasco, A.; Lippard, S. J. *Biochemistry* **1998**, *37*, 9230.

(16)   Elizondo-Riojas, M. A.; Kozelka, J. *J. Mol. Biol.* **2001**, *314*, 1227.

(17)   Zhu, Y. Y.; Wang, Y.; Chen, G. J. *Nucleic Acids Res.* **2009**, *37*, 5930.

(18)   Teletchea, S.; Skauge, T.; Sletten, E.; Kozelka, J. *Chem. Eur. J.* **2009**, *15*, 12320.

(19)   Barnham, K. J.; Bernersprice, S. J.; Frenkiel, T. A.; Frey, U.; Sadler, P. J. *Angew. Chem. Int. Ed.* **1995**, *34*, 1874.

(20)   Parkinson, J. A.; Chen, Y.; Murdoch, P. D.; Guo, Z. J.; Berners-Price, S. J.; Brown, T.; Sadler, P. J. *Chem. Eur. J.* **2000**, *6*, 3636.

(21)   Chen, Y.; Parkinson, J. A.; Guo, Z. J.; Brown, T.; Sadler, P. J. *Angew. Chem. Int. Ed.* **1999**, *38*, 2060.

(22)   Farrer, N. J.; Woods, J. A.; Salassa, L.; Zhao, Y.; Robinson, K. S.; Clarkson, G.; Mackay, F. S.; Sadler, P. J. *Angew. Chem. Int. Ed.* **2010**, 8905.

(23)   Natile, G.; Coluccia, M. *Coord. Chem. Rev.* **2001**, *216*, 383.

(24)   Mackay, F. S.; Woods, J. A.; Heringova, P.; Kasparkova, J.; Pizarro, A. M.; Moggach, S. A.; Parsons, S.; Brabec, V.; Sadler, P. J. *Proc. Natl. Acad. Sci. USA* **2007**, *104*, 20743.

(25)   Wu, B.; Davey, C. A. *Chem. Biol.* **2008**, *15*, 1023.

(26)   Ober, M.; Lippard, S. J. *J. Am. Chem. Soc* **2008**, *130*, 2851.

(27)   Ober, M.; Lippard, S. J. *J. Am. Chem. Soc.* **2007**, *129*, 6278.

(28)   Galea, A. M.; Murray, V. *Chem. Biol. Drug Design* **2010**, *75*, 578.

(29)   Allen, M.; Tildesley, D. *Computer simulation of liquids*; Oxford University Press, USA, 1990.

(30)   Hambley, T. W.; Jones, A. R. *Coord. Chem. Rev.* **2001**, *212*, 35.

34

(31)   Burton, V. J.; Deeth, R. J.; Kemp, C. M.; Gilbert, P. J. *J. Am. Chem. Soc.* **1995**, *117*, 8407.

(32)   Deeth, R. J. *Coord. Chem. Rev.* **2001**, *212*, 11.

(33)   Deeth, R.; Anastasi, A.; Diedrich, C.; Randell, K. *Coord. Chem. Rev.* **2009**, *253*, 795.

(34)   Piquemal, J. P.; Williams-Hubbard, B.; Fey, N.; Deeth, R. J.; Gresh, N.; Giessner-Prettre, C. *J. Comput. Chem.* **2003**, *24*, 1963.

(35)   Woodley, S. M.; Battle, P. D.; Catlow, C. R. A.; Gale, J. D. *J. Phys. Chem. B* **2001**, *105*, 6824.

(36)   Deeth, R. J. *Chem. Commun.* **2006**, 2551.

(37)   Chval, Z.; Sip, M. *J. Phys. Chem. B* **1998**, *102*, 1659.

(38)   Anastasi, A.; Deeth, R. J. *J. Chem. Theory. Comput.* **2009**, *5*, 2339.

(39)   Noll, D. M.; Mason, T. M.; Miller, P. S. *Chem. Rev.* **2006**, *106*, 277.

(40)   E.J. Baerends, et al. Amsterdam Density Functional 2007.01, SCM, Vrije Universiteit, Amsterdam, The Netherlands: Amsterdam, 2007.

(41)   Becke, A. *Phys. Rev. A* **1988**, *38*, 3098.

(42)   Perdew, J. *Phys. Rev. B* **1986**, *33*, 8822.

(43)   Grimme, S. *J. Comp. Chem.* **2004**, *25*, 1463.

(44)   van Lenthe, E.; Ehlers, A.; Baerends, E. *J. Chem. Phys.* **1999**, *110*, 8943.

(45)   Chirlian, L. E.; Francl, M. M. *J. Comput. Chem.* **1987**, *8*, 894.

(46)   Frisch, M.; Trucks, G.; Schlegel, H.; Scuseria, G.; Robb, M.; Cheeseman, J.; Montgomery Jr, J.; Vreven, T.; Kudin, K.; Burant, J. In *Gaussian 2003*; Revision B. 05, Gaussian, Inc.: Pittsburgh, PA, 2003.

(47)   Hay, P. J.; Wadt, W. R. *J. Chem. Phys.* **1985**, *82*, 299.

(48)   Ehlers, A.; Böhme, M.; Dapprich, S.; Gobbi, A.; Höllwarth, A.; Jonas, V.; Köhler, K.; Stegmann, R.; Veldkamp, A.; Frenking, G. *Chem. Phys. Lett.* **1993**, *208*, 111.

(49)   Figgis, B. N.; Hitchman, M. A. *Ligand field theory and its applications*; Wiley-VCH: New York [etc.], 2000.

(50)   Deeth, R. J.; Foulis, D. L. *PCCP* **2002**, *4*, 4292.

(51)   Deeth, R. J.; Fey, N.; Williams-Hubbard, B. J. *J. Comp. Chem.* **2005**, *26*, 123.

(52)   A copy of DommiMOE can be obtained from the authors. Certain conditions apply.

(53)   Halgren, T. A. *J. Comput. Chem.* **1996**, *17*, 490.

(54)   Halgren, T. A. *J. Comput. Chem.* **1996**, *17*, 520.

(55)   Halgren, T. A. *J. Comput. Chem.* **1996**, *17*, 553.

(56)   Halgren, T. A.; Nachbar, R. B. *J. Comput. Chem.* **1996**, *17*, 587.

(57)   Halgren, T. A. *J. Comput. Chem.* **1996**, *17*, 616.

(58)   Pearlman, D. A.; Case, D. A.; Caldwell, J. W.; Ross, W. S.; Cheatham, T. E.; DeBolt, S.; Ferguson, D.; Seibel, G.; Kollman, P. *Comput. Phys. Commun.* **1995**, *91*, 1.

(59)   Brooks, B. R.; Bruccoleri, R. E.; Olafson, B. D.; States, D. J.; Swaminathan, S.; Karplus, M. *J. Comput. Chem.* **1983**, *4*, 187.

(60)   Ryckaert, J.-P.; Ciccotti, G.; Berendsen, H. J. C. *J. Comput. Phys.* **1977**, *23*, 327.

(61)   Smith, W.; Yong, C. W.; Rodger, P. M. *Mol. Sim.* **2002**, *28*, 385.

35

(62)   DL_POLY_LF implements the standard molecular form of LFMM as described in reference 61. Stress tensor components are computed for all interactions except the d-electron energy.

(63)   Lovejoy, K. S.; Todd, R. C.; Zhang, S. Z.; McCormick, M. S.; D'Aquino, J. A.; Reardon, J. T.; Sancar, A.; Giacomini, K. M.; Lippard, S. J. *Proc. Natl. Acad. Sci. USA* **2008**, *105*, 8902.

(64)   Brabec, V.; Reedijk, J.; Leng, M. *Biochemistry* **1992**, *31*, 12397.

(65)   Kasparkova, J.; Zehnulova, J.; Farrell, N.; Brabec, V. *J. Biol. Chem.* **2002**, *277*, 48076.

(66)   Kasparkova, J.; Novakova, O.; Marini, V.; Najajreh, Y.; Gibson, D.; Perez, J.-M.; Brabec, V. *J. Biol. Chem.* **2003**, *278*, 47516.

(67)   Leng, M.; Locker, D.; Giraud-Panis, M. J.; Schwartz, A.; Intini, F. P.; Natile, G.; Pisano, C.; Boccarelli, A.; Giordano, D.; Coluccia, M. *Mol. Pharmacol.* **2000**, *58*, 1525.

(68)   Comess, K. M.; Costello, C. E.; Lippard, S. J. *Biochemistry* **1990**, *29*, 2102.

(69)   Lemaire, M. A.; Schwartz, A.; Rahmouni, A. R.; Leng, M. *Proc. Natl. Acad. Sci. USA* **1991**, *88*, 1982.

(70)   Brabec, V.; Leng, M. *Proc. Natl. Acad. Sci. USA* **1993**, *90*, 5345.

(71)   Kasparkova, J.; Mellish, K. J.; Qu, Y.; Brabec, V.; Farrell, N. *Biochemistry* **1996**, *35*, 16705.

(72)   Zakovska, A.; Novakova, O.; Balcarova, Z.; Bierbach, U.; Farrell, N.; Brabec, V. *Eur. J. Biochem.* **1998**, *254*, 547.

(73)   Brabec, V.; Neplechova, K.; Kasparkova, J.; Farrell, N. *J. Biol. Inorg. Chem.* **2000**, *5*, 364.

(74)   Bancroft, D. P.; Lepre, C. A.; Lippard, S. J. *J. Am. Chem. Soc.* **1990**, *112*, 6860.

(75)   Draganescu, A.; Tullius, T. D. In *Met. Ions Biol. Syst.*; Sigel, A., Sigel, H., Eds.; Marcel Dekker, Inc.: New York, 1996; Vol. 33, p 453.

(76)   Maxam, A. M.; Gilbert, W. *Methods Enzymol.* **1980**, *65*, 499.

(77)   Cornell, W. D.; Cieplak, P.; Bayly, C. I.; Gould, I. R.; Merz, K. M.; Ferguson, D. M.; Spellmeyer, D. C.; Fox, T.; Caldwell, J. W.; Kollman, P. A. *J. Am. Chem. Soc.* **1995**, *117*, 5179.

(78)   Allen, F. *Acta Crystallogr. Sect. B: Struct. Sci.* **2002**, *58*, 380.

(79)   Sherman, S.; Gibson, D.; Wang, A.; Lippard, S. *Science* **1985**, *230*, 412.

(80)   Coll, M.; Sherman, S.; Gibson, D.; Lippard, S.; Wang, A. *J. Biomol. Struct. Dynamics* **1990**, *8*, 315.

(81)   Gkionis, K.; Platts, J. *J. Biol. Inorg. Chem.* **2009**, *14*, 1165.

(82)   Deeth, R. J.; Diedrich, C. *J. Biol. Inorg. Chem.* **2010**, *15*, 117.

(83)   Spiegel, K.; Rothlisberger, U.; Carloni, P. *J. Phys. Chem. B* **2004**, *108*, 2699.

(84)   Deeth, R. J. *Inorg. Chem.* **2007**, *46*, 4492.

(85)   Deeth, R. J.; Randell, K. *Inorg. Chem.* **2008**, *47*, 7377.

(86)   Lavery, R.; Moakher, M.; Maddocks, J.; Petkeviciute, D.; Zakrzewska, K. *Nucleic Acids Res.* **2009**, *37*, 5917.

(87)   Kartalou, M.; Essigmann, J. M. *Mutation Research* **2001**, *478*, 1.

(88)   Rohs, R.; West, S. M.; Sosinsky, A.; Liu, P.; Mann, R. S.; Honig, B. *Nature* **2009**, *461*, 1248.

36

Table of contents graphic
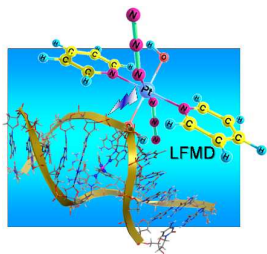
The major Pt(II) photoproduct from *trans,trans,trans* –[Pt(N$_3$)$_2$(OH)$_2$(pyridine)] is shown experimentally to bind DNA via a variety of crosslinks including the *trans*-{Pt(pyridine)$_2$} moiety coordinated to the N7 positions of guanines on different DNA strands. Ligand field molecular mechanics has been extented to Pt(II)-N(guanine) bonds and used in dynamics simulations to characterize atomistically this novel platinated lesion and gain some insights into its high anti-cancer potency.

37